Dalton Transactions

ROYAL SOCIETY OF CHEMISTRY

PAPER

View Article Online
View Journal | View Issue

Cite this: *Dalton Trans.*, 2024, **53**, 14182

Engineering VO_x structure by integrating oxygen vacancies for improved zinc-ion storage based on cation-doping regulation with electric density†

Juan Xu, * Nengneng Han, Sihao Chen, Yahui Zhang, Yuezhou Jing, Pibin Bing and Zhongyang Li*

Received 14th May 2024,
Accepted 25th July 2024

DOI: 10.1039/d4dt01415d

rsc.li/dalton

Aqueous zinc-ion batteries (ZIBs) have attracted enormous attention for future energy-storage devices owing to their high theoretical capacity and environmental friendliness. However, obtaining cathodes with a high specific capacity and fast reaction kinetics remains a huge challenge. Herein, Cu-VO_x material with a thin sheet microsphere structure composed of nanoparticles was prepared by a simple hydrothermal reaction, which improved reaction kinetics and specific capacity. Pre-embedding Cu^{2+} into V_2O_5 to introduce abundant oxygen vacancies extended the interlayer distance to 1.16 nm, weakened the effect of the V–O bonds, and improved the electrical conductivity and structural stability. At the same time, the influence of different valence metal ions (M = K^+, Cu^{2+}, Fe^{3+}, Sn^{4+}, Nb^{5+}, and W^{6+}) pre-embedded in V_2O_5 was studied. Benefiting from a large interlayer spacing, high electrical conductivity, and excellent structural stability, the Cu-VO_x electrode demonstrated a high specific capacity of 455.9 mA h g^{-1} at 0.1 A g^{-1}. Importantly, when the current density was increased to 6 A g^{-1}, the Cu-VO_x electrode still achieved a high specific capacity of 178.8 mA h g^{-1} and maintained a high capacity retention of 76.5% over 2000 cycles.

1. Introduction

With the rapid development of the economy, the use of non-renewable energy (including natural gas, crude oil, and carbon) has also increased significantly, making the development of renewable energy imminent. In recent years, lithium-ion batteries have been widely used in the field of electric vehicles due to their high energy density.[1–4] However, the organic electrolyte in commercial lithium-ion batteries is flammable, which has resulted in several fire accidents in electric vehicles and limited the future use of lithium-ion batteries for energy storage.[5–7] Whereas, aqueous zinc-ion batteries, with a suitable redox potential of −0.76 V *vs.* hydrogen electrode and high theoretical specific capacity up to 820 mA h g^{-1} (5854 mA h cm^{-3}), are a safer and more stable alternative to lithium-ion batteries, making them the most promising energy-storage devices.[8–11]

Similar to lithium-ion batteries, the cathode material is critical to determine the performance of aqueous zinc-ion batteries. Vanadium-based oxides, manganese-based oxides, and Prussian blue analogs are the most commonly utilized cathode materials for zinc-ion batteries.[12–16] Vanadium-based materials, such as vanadium pentoxide, have attracted considerable attention for their use in aqueous zinc-ion batteries owing to the merits of a layered structure and high specific capacity.[17–19] However, limitations, such as a lower average voltage and a structure that is prone to collapse during the charging/discharging cycling process, have hindered the development of vanadium-based materials.[14,20] In order to address the previous difficulties, researchers have implemented an ion pre-embedding technique to resolve the poor rate performance and sluggish reaction kinetics caused by the irreversible phase changes in their crystal structure. Pre-embedding metal ions not only increases the layer spacing of vanadium-based materials and promotes fast ion diffusion but also works as a "pillar" to improve the overall stability of the materials.[21–23] For example, Tong *et al.* employed a pre-intercalation technique involving iron and alkylammonium ions to create FeVO-12 composites effectively. The FeVO-12 compounds exhibited exceptional surface hydrophobicity and structural stability due to the combined influence of the two ions. The FeVO-12 electrode displayed a reversible specific capacity of 408 mA h g^{-1} at a current density of 0.1 A g^{-1}. In addition, even after undergoing 1000 cycles at a high current density of 10 A g^{-1}, the electrode maintained a high capacity retention rate of 90%.[24] Pang *et al.* successfully synthesized the new cathode material $Mn_{0.2}V_8O_{20}\cdot1.12H_2O$ (MnVO) using a hydrothermal reaction. The inclusion of water molecules and Mn^{2+}

School of Electrical College, North China University of Water Resources and Electric Power, Zhengzhou 450045, P. R. China. E-mail: xujuan@ncwu.edu.cn, thzwave@163.com

† Electronic supplementary information (ESI) available. See DOI: https://doi.org/10.1039/d4dt01415d

in the interlayer effectively helped avoid collapse of the cathode structure. The MnVO cathode exhibited a high specific capacity of 306.4 mA h g^{-1} at a current density of 0.1 A g^{-1}. It also demonstrated a capacity retention of 86.4% after 1000 charging/discharging cycles at a current density of 2.0 A g^{-1}, demonstrating its excellent cycling stability.[25] Qi's group investigated a cesium ion-inserted vanadium oxide nanorod (CsVO) as the cathode for zinc-ion batteries, which exhibited excellent electrochemical properties. The embedded cesium ions formed strong Cs–O bonds with oxygen atoms, while Cs doping made the interlayer interaction stronger. As a result, the Cs^+-intercalated material demonstrated excellent multiplicity performances and an ultra-long cycling lifespan. The CsVO electrode showed a high specific capacity of 189.9 mA h g^{-1} at 20 A g^{-1}. Also, it exhibited outstanding cycling stability with 89% capacity retention over more than 10 000 cycles at a high current density of 20 A g^{-1}.[26] Metal ions pre-embedded in vanadium oxides improve the electrical conductivity and structural stability, which is further strengthened by the strong coordination bonds established between the metal ions and oxygen atoms. Although the strategy of improving the electrochemical properties of vanadium oxides by pre-embedding various metal ions (Mg^{2+}, Mn^{2+}, Ca^{2+}, K^+, Fe^{3+}, Zn^{2+}, and Al^{3+})[27–32] has been extensively reported, the effect of ionic bonds formed between metal cations with different valence states and the host structure on the electrochemical properties of vanadium oxides remains unknown.

Based on the above considerations, we designed and prepared M-doped V_2O_5 (M-VO_x) with metal ions in different valence states. The doping of metal ions into V_2O_5 enlarged the interlayer spacing to shorten the diffusion distance for Zn^{2+}. Importantly, Cu-VO_x materials with a thin sheet microsphere structure composed of nanoparticles were successfully prepared, with the largest interlayer distance of 1.16 nm. In addition, pre-embedding Cu^{2+} into V_2O_5 could introduce abundant oxygen vacancies to improve the electrical conductivity, weaken the effect of V–O bonds, and enhance the structural stability. As expected, the Cu-VO_x electrode achieved a high specific capacity of 455.9 mA h g^{-1} at 0.1 A g^{-1}, a favorable rate capacity of 178.8 mA h g^{-1} at a high current density of 6 A g^{-1}, and a high capacity retention of 76.5% after 2000 charging/discharging cycles, which demonstrated its promising cycling stability. Hence, the strategy of doping metal ions with the optimal electrical density can effectively improve the electrochemical performance of metal compounds through a synergistic effect, providing a new route for constructing aqueous zinc-ion batteries with high energy density.

2. Experimental section

2.1 Materials

Vanadium pentoxide (V_2O_5), potassium chloride (KCl), copper chloride dihydrate ($CuCl_2{\cdot}2H_2O$), ferric chloride hexahydrate ($FeCl_3{\cdot}6H_2O$), tin chloride pentahydrate ($SnCl_4{\cdot}5H_2O$), niobium chloride ($NbCl_5$), tungsten chloride (WCl_6), hydrogen peroxide (H_2O_2), zinc foil, and zinc trifluoromethyl sulfonate ($Zn(CF_3SO_3)_2$) were purchased from Sinopharm Co. LTD. The deionized water (DI) used in the experiment was ultrapure water. All the raw materials were of analytical grade and used without further purification.

2.2 Materials synthesis

Various metal-ion-doped M-VO_x materials were prepared by a green and pollution-free one-step hydrothermal method. Taking the preparation procedure for Cu-VO_x materials as an example. Initially, the precursor solution was prepared by dissolving 2 mol V_2O_5 into 50 ml deionized water. Subsequently, 2 mol $CuCl_2{\cdot}2H_2O$ was added to the solution and the solution was agitated constantly until it was fully dissolved. Subsequently, 2 ml hydrogen peroxide (H_2O_2) was incrementally introduced into the solution dropwise while stirring for 30 min. Subsequently, the solution was put into a high-pressure reactor with a volume of 100 ml. The reaction was then conducted at 200 °C for 48 h. After cooling to room temperature, the obtained products were cleaned with deionized water and ethanol three times, respectively, and then dried at 80 °C. Also, K-VO_x, Fe-VO_x, Sn-VO_x, Nb-VO_x, and W-VO_x materials were prepared using the same method as described above, with the only difference being the substitution of $CuCl_2{\cdot}2H_2O$ with KCl, $FeCl_3{\cdot}6H_2O$, $SnCl_4{\cdot}5H_2O$, $NbCl_5$, or WCl_6 powder, respectively.

2.3 Characterization

The samples' surface morphology was characterized by scanning electron microscopy (SEM) and high-resolution transmission electron microscopy (HRTEM, Tecnai G20). Their chemical structures were analyzed by powder X-ray diffraction (XRD) with Cu Kα radiation (λ = 1.54118 Å) and X-ray photoelectron spectroscopy (XPS). A specific surface area analyzer (BET) (JWBK100) was used to characterize the specific surface area and pore-size distribution of the materials.

2.4 Electrochemical measurements

CR2025 coin cells were used to characterize the electrochemical properties of the materials. Here, the active material, conductive carbon black (Super-P), and polyvinyl tetrafluoroethylene (PVDF) were dissolved in a certain amount of *N*-methyl-2-pyrrolidone (NMP) solvent in a mass ratio of 7 : 2 : 1 and the solution was stirred at room temperature to obtain a homogeneous slurry. Then, the prepared slurry was scatter-coated on the carbon paper collector and after vacuum-dried at 80 °C overnight to prepare the working electrode. The prepared working electrode was used as the cathode, pretreated zinc foil was used as the anode, the Whatman membrane was used as the separator, and 3 M $Zn(CF_3SO_3)_2$ solution was used as the electrolyte to assemble button-type aqueous zinc-ion batteries in the air. Among these, the active material loading of the working electrode was 1–2 mg. We tested the zinc-ion batteries using cyclic voltammetry (CV), galvanostatic charge–discharge (GCD), and electrochemical impedance spectroscopy (EIS) using an electrochemical workstation (CHI

660E, Shanghai, China) and battery test system (LAND, CT2001, Shanghai, China).

3. Results and discussion

Cu-VO_x compounds were prepared as shown schematically in Fig. 1 by a one-step hydrothermal method (see the Experimental section for details).

The morphologies of the Cu-VO_x, K-VO_x, Fe-VO_x, Sn-VO_x, Nb-VO_x, and W-VO_x compounds were characterized by scanning electron microscopy (SEM) and transmission electron microscopy (TEM). Fig. 2a shows that the Cu-VO_x material had a relatively dense microsphere structure due to the polymerization of several nanosheets with a diameter of about 4 μm. Further characterization revealed that the nanosheets were composed of many uniform nanoparticles with a diameter of about 2–5 nm (Fig. 2b). This ultra-small nanoparticles structure is conducive to electrolyte penetration into the electrode material, shortening the ion-diffusion distance and enhancing the structural stability.[33–35] The TEM images in Fig. 2c also confirmed the thin sheet morphology of the surface of the Cu-VO_x microspheres. In addition, Fig. S1† shows the morphology of the contrast samples. Among these, the K-VO_x materials were composed of nanorods with a length of about 1 μm, and some nanorods showed a curved morphology. These relatively thick and stacked nanorods make it difficult to maintain structural stability during electrochemical reactions. The Sn-VO_x materials also showed a nanorod structure, with a length of about 2 μm and a partial sheet form, which was formed by stacking nanorods. The Nb-VO_x materials had a thick nanosheets structure, which randomly stacked

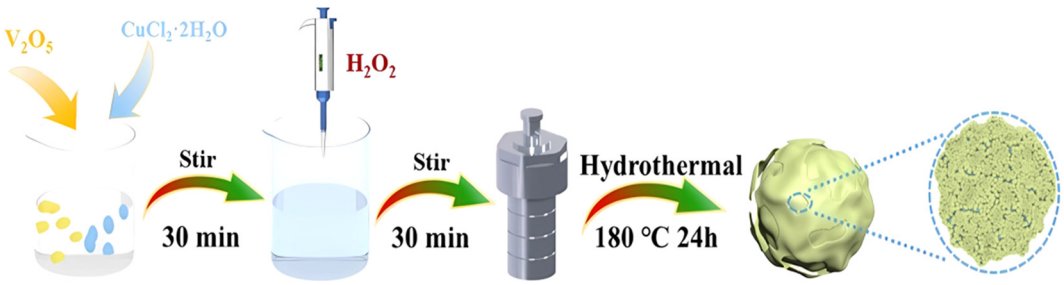

Fig. 1 Schematic diagram for the preparation of the Cu-VO_x compounds.

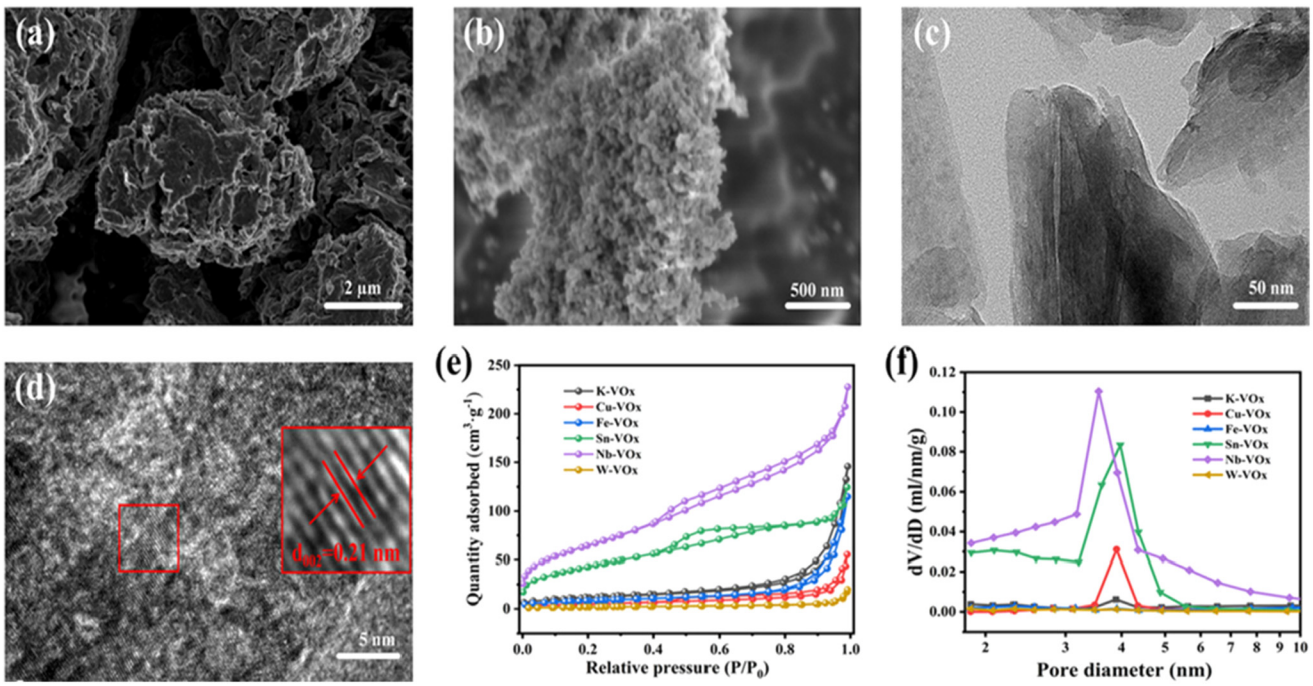

Fig. 2 (a and b) SEM images of the Cu-VO_x compounds at different magnifications; (c) TEM and (d) HRTEM images of the Cu-VO_x compounds; (e and f) N_2 adsorption–desorption curves and pore-size distribution curves of the Cu-VO_x, K-VO_x, Fe-VO_x, Sn-VO_x, Nb-VO_x, and W-VO_x materials, respectively.

together, which was not conducive to the rapid transport of ions. The Fe-VO_x materials displayed a nanoblock structure with multiple layers of nanosheets stacked on each other, which could easily collapse during the process of embedding Zn^{2+}. The W-VO_x materials also had a nanoblock structure stacked with multiple nanosheets, and the nanoblocks were larger, making it more difficult to maintain structural stability during zinc-ion transport.[36] Obviously, the thin sheet microsphere structure presented by Cu-VO_x materials composed of nanoparticles could shorten the transport path of zinc ions, maintain the structural stability, and support excellent electrochemical performances, which was also consistent with the analysis of the electrochemical performance. Fig. 2d shows a HRTEM image of Cu-VO_x with a lattice spacing of 0.21 nm, corresponding to the (002) crystal faces of VO_x (JCPDS 41-1426). Fig. 2e and f show the BET adsorption–desorption curves and pore-size distribution curves of Cu-VO_x, K-VO_x, Sn-VO_x, Nb-VO_x, Fe-VO_x, and W-VO_x, respectively. Their specific surface areas were 18.48, 41.73, 30.24, 157.42, 236.63, and 7.16 $m^2\ g^{-1}$, respectively, and their pore sizes were distributed at about 3–4 nm. The results showed that the embedding of different valence metal ions had little effect on the pore-size distribution of VO_x materials but had a greater effect on the specific surface area. The large specific surface area of Cu-VO_x materials increased the contact area of the electrolyte and the electrode surface, and improved zinc-ion transport, which were conducive to the improvement of the electrochemical performances.[37,38]

XRD measurements were used to characterize the effects of different valence ions on the crystal structure of the VO_x materials (Fig. 3a). Among these, the K-VO_x, Cu-VO_x, and Nb-VO_x samples showed strong diffraction peaks for the (001) crystal plane at $2\theta = 7.29°$, indicating that K^+, Cu^{2+}, and Nb^{5+} had been successfully embedded in the interlayer of the VO_x material. Using Bragg's formula, it was calculated that the crystal plane spacing of Cu-VO_x increased from 0.44 nm to 1.16 nm, and the ion embedding not only increased the layer spacing but also improved the structural stability of the material.[39] However, no discernible diffraction peaks were seen at $2\theta = 7.29°$ in the XRD patterns of the Sn-VO_x, Fe-VO_x, and W-VO_x materials. This perhaps could be attributed to the inability of Sn^{4+}, Fe^{3+}, and W^{5+} to considerably enhance the interlayer spacing of the materials when integrated into the VO_x materials. Furthermore, the XRD patterns of the materials did not exhibit any new phases upon embedding the ions with varying valence states in the VO_x materials. Next, X-ray photoelectron spectroscopy (XPS) analysis of the VO_x materials was performed and confirmed that Cu^{2+} was indeed embedded in the VO_x material (Fig. 3b); whereby the strong peaks that arose at binding energies of 932.3 and 952.3 eV in the Cu 2p XPS spectrum in Fig. 3c corresponded to Cu $2p_{3/2}$ and Cu $2p_{1/2}$, respectively. This suggested that the majority of the ions

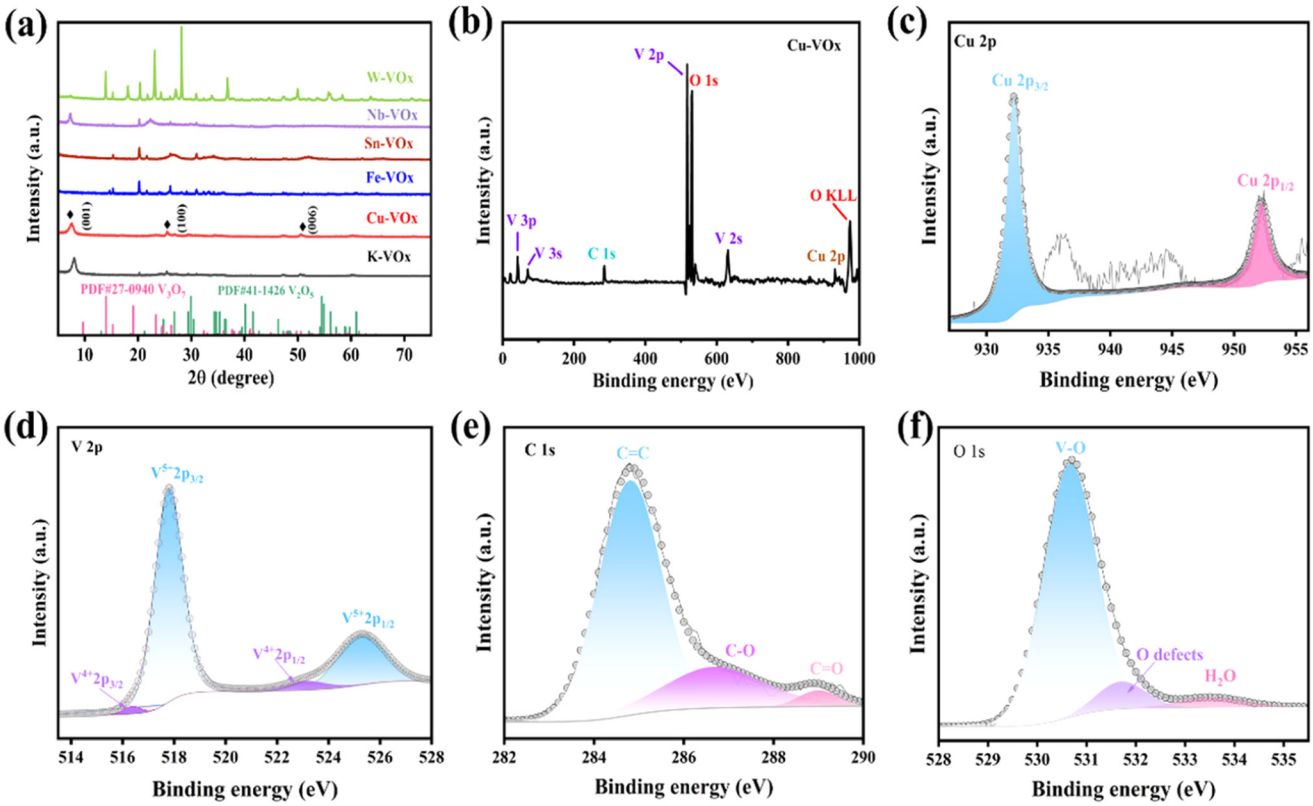

Fig. 3 (a) XRD spectra of the Cu-VO_x, K-VO_x, Fe-VO_x, Sn-VO_x, Nb-VO_x, and W-VO_x materials, respectively. (b, c, d, e and f) Full XPS spectrum, and Cu 2p, V 2p, C 1s, and O 1s spectra of the Cu-VO_x materials, respectively.

buried in Cu-VO_x were Cu^{2+}. The V 2p XPS spectrum of the Cu-VO_x material is displayed in Fig. 3d. The V(5+)–O stretching-related diffraction peaks with binding energies of 517.8 and 525.2 eV corresponded to V^{5+} $2p_{3/2}$ and V^{5+} $2p_{1/2}$, respectively.[40] Furthermore, there were peaks at binding energies of 516.4 and 523.1 eV, which subsequently corresponded to V^{4+} $2p_{3/2}$ and V^{4+} $2p_{1/2}$, respectively. The analysis mentioned above demonstrated that the Cu-VO_x material had a low valence state of V^{4+} and considerable V^{5+}. According to the charge-conservation principle, oxygen vacancies must be created in the V_2O_5 lattice to make up for the charge neutralization.[41,42] The XPS spectrum of C 1s is shown in Fig. 3e, displaying pronounced peaks at 284.8, 286.7, and 289 eV, corresponding to C═C, C–O and C═O bonds, respectively.[43] In the O 1s XPS spectrum in Fig. 2f, three obvious diffraction peaks at binding energies of 530.7, 531.7, and 533.5 eV could be seen, corresponding to lattice oxygen, oxygen vacancies, and adsorbed oxygen, respectively, further confirming the existence of oxygen vacancies, in which the proportion of oxygen vacancies was about 14.19%.[26] Incorporating Cu^{2+} into VO_x could increase the lattice spacing and introduce abundant oxygen vacancies. Benefiting from the synergistic effect, the Cu-VO_x materials exhibited enhanced structural stability, high electrical conductivity, and excellent electrochemical performances.

The electrochemical performances of the Cu-VO_x electrode and the contrast electrodes were studied with coin cells, in which the working electrodes, zinc foil, 3 M Zn $(CF_3SO_3)_2$ electrolyte, and Whatman membrane served as the cathode, anode, electrolyte, and separator, respectively. Fig. 4a displays the cyclic voltammetry (CV) curves of the Cu-VO_x electrode at a scan rate of 0.1 mV s^{-1} during the initial five cycles. The CV curves for the initial five cycles showed similar patterns, suggesting the significant electrochemical reversibility of the Cu-VO_x electrode. Furthermore, the CV curves of Cu-VO_x exhibited two pair of redox peaks at 0.63/1.02 and 0.51/0.91 V. These peaks corresponded to the oxidation–reduction reactions of V^{5+}/V^{4+} and V^{4+}/V^{3+}, respectively.[44,45] For contrast, Fig. S2† shows the CV curves of the K-VO_x, Fe-VO_x, Sn-VO_x, Nb-VO_x, and W-VO_x electrodes. Among these, the CV curves of the Cu-VO_x electrode had the largest area, indicating that the Cu-VO_x electrode exhibited the relatively largest specific capacity. In the CV curves of the contrast electrodes, two pairs of obvious redox peaks were observed in all, and the corresponding voltage positions were basically the same. This indicated that the metal ions embedded in VO_x increased the interlayer distance and electrical conductivity of the materials, but the contribution to the increase in the redox active sites was relatively weak, which was consistent with the analysis showing that the Cu-VO_x, K-VO_x, and Nb-VO_x electrodes had relatively high specific capacities. Fig. 4b displays the galvanostatic charge–discharge (GCD) curves for the Cu-VO_x, K-VO_x, Sn-VO_x, Nb-VO_x, Fe-VO_x, and W-VO_x electrodes at a current density of 0.1 A g^{-1}, with all showing a pronounced redox plateau. Also, the results were also consistent with the analyses of the CV curves in Fig. 4a and Fig. S2.† It is obvious that the Cu-VO_x electrode had a higher specific capacity. The GCD curves of the Cu-VO_x electrode at different current densities are shown in Fig. 4c. The Cu-VO_x electrodes achieved specific capacities of 455.9, 395.8, 373.2, 356.7, 339.2, 319.8, 248.1, 171.7, 126.7, and 97.9 mA h g^{-1} at varied current densities of 0.1, 0.2, 0.4, 0.6, 0.8, 1.0, 2.0, 4.0, 6.0, and 8.0 A g^{-1}, respectively, demonstrating the electrodes outstanding rate properties. When the current density was recovered to 0.1 A g^{-1}, the Cu-VO_x electrode could still obtain a high specific capacity of 399.8 mA h g^{-1} with a capacity retention of nearly 87.7%, indicating that that Cu-VO_x electrode had excellent reversibility and cycling stability during the charging/discharging process. Fig. 4d shows the rate characteristics of the contrast electrodes at various current densities. Obviously, the rate characteristics of the Cu-VO_x electrode were much better than those of the contrast electrodes. (The values of the current densities are marked on the graph.) Compared with the contrast materials, the bonding cooperation of V–O bonds in the Cu-VO_x electrode was stronger, and thus the structure was more stable. The cycling stability of different electrodes at 0.1 A g^{-1} was further investigated, as shown in Fig. 4e. The Cu-VO_x electrode still obtained a high specific capacity of 300 mA h g^{-1} after 200 charging/discharging cycles, showing its excellent cycling stability. In addition, the Fe-VO_x, Sn-VO_x, Nb-VO_x, and W-VO_x electrodes showed poor cycling stability with lower initial specific capacities in the first 30 cycles and a large decrease in specific capacity with increasing the cycling number, which could be attributed to the collapse of the nanoblock structure and the slow activation process. Interestingly, the specific capacity of the K-VO_x electrode decreased from an initial 423.4 mA h g^{-1} to 246.3 mA h g^{-1} after 30 cycles at 0.1 A g^{-1}, and then the capacity slowly increased in the subsequent cycles, which may be due to the gradual activation process of the material. The Cu-VO_x electrode demonstrated excellent cycling stability in the charging/discharging cycles, which could be attributed to the increased interlayer distance and high electrical conductivity. Moreover, the lamellar microsphere structure consisting of nanoparticles shortened the ion-transport distance, improved the structural stability, accelerated the electrochemical activation process, and increased the redox kinetics rate.[46–49] The reaction kinetics of the Cu-VO_x, K-VO_x, Sn-VO_x, Nb-VO_x, Fe-VO_x, and W-VO_x electrodes were analyzed using electrochemical impedance spectroscopy (EIS), respectively, as shown in Fig. 4f. In the equivalent circuit, R_s represents the Ohmic resistance, R_{ct} represents the charge-transfer resistance, Z_w denotes the Warburg impedance of Zn^{2+} diffusion into the bulk phase of the active material, and Q is the constant-phase angle.[37] The Cu-VO_x electrode exhibited a smaller charge-transfer resistance, as shown in Fig. 4f, indicating that the Cu-VO_x electrode had an optimal electrical conductivity, which was mainly attributed to the pre-embedding of Cu^{2+} to introduce abundant oxygen vacancies in the Cu-VO_x material. Fig. 4g shows that the Cu-VO_x electrode had a high initial capacity of 178.8 mA h g^{-1} at a high current density of 6 A g^{-1}, and kept a specific capacity of 136.7 mA h g^{-1} after 2000 cycles with a high capacity retention of 76.5%. This indicated that the Cu-VO_x electrode had excellent cycling stability at high current density, which could be attributed to

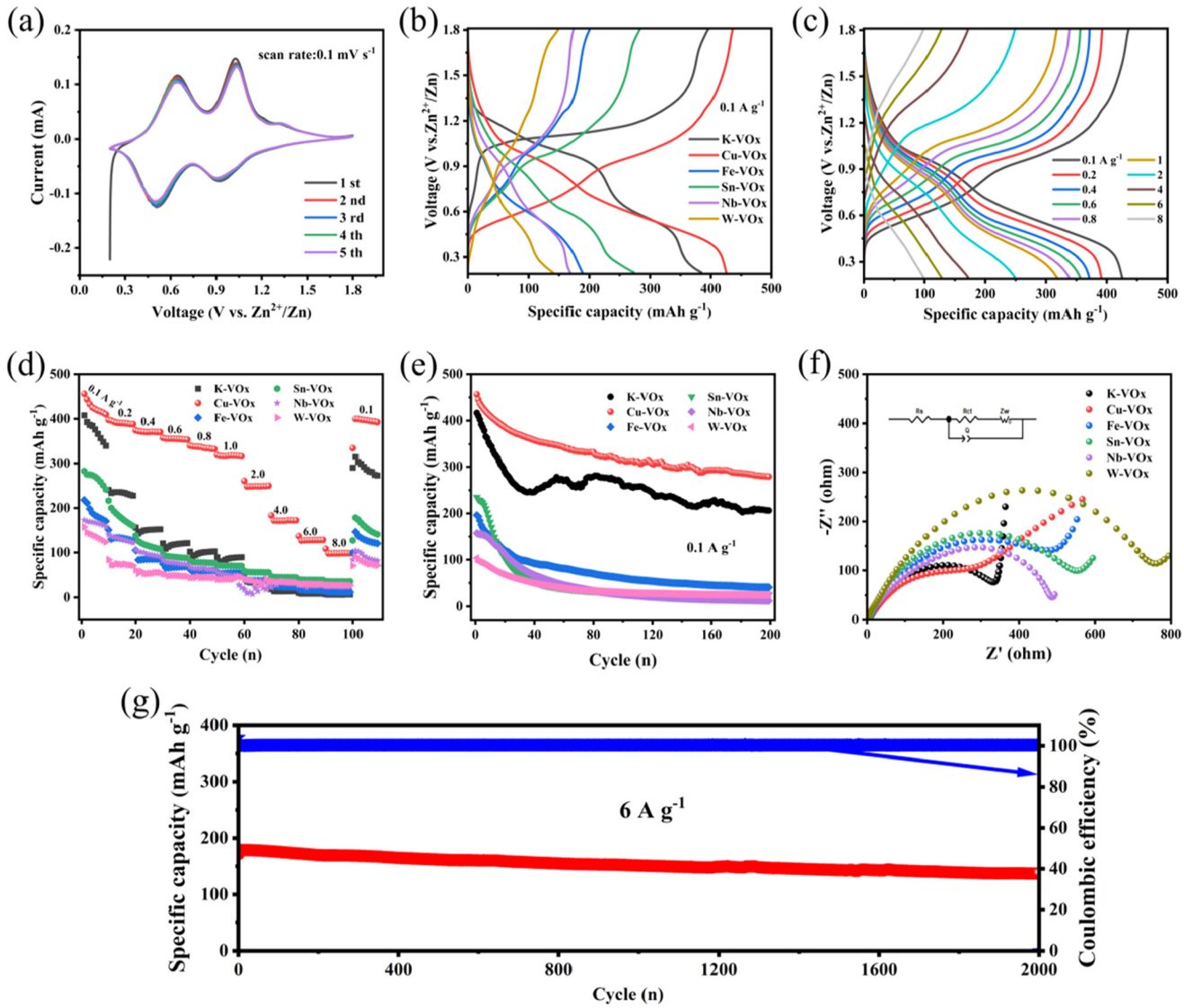

Fig. 4 (a) First five cyclic voltammetry (CV) curves of the Cu-VO_x electrode at 0.1 mV s^{-1}; (b) GCD curves of the Cu-VO_x, K-VO_x, Fe-VO_x, Sn-VO_x, Nb-VO_x, and W-VO_x electrodes at a current density of 0.1 A g^{-1}, respectively; (c) GCD curves of the Cu-VO_x electrode at various current densities ranging from 0.1 to 8 A g^{-1}; (d) rate capacity of the Cu-VO_x, K-VO_x, Fe-VO_x, Sn-VO_x, Nb-VO_x, and W-VO_x electrodes at different current densities; (e) cycling performances of the Cu-VO_x, K-VO_x, Fe-VO_x, Sn-VO_x, Nb-VO_x, and W-VO_x electrodes at 0.1 A g^{-1}; (f) Nyquist plots of the Cu-VO_x, K-VO_x, Fe-VO_x, Sn-VO_x, Nb-VO_x, and W-VO_x electrodes; (g) cycling performance of the Cu-VO_x electrode at a high current density of 6 A g^{-1}.

the lamellar microsphere structure of the Cu-VO_x material consisting of nanoparticles, demonstrating its outperforming structural stability.

To further study the synergistic effect of abundant oxygen vacancies and metal ion pre-embedding to improve the electrochemical performance of the electrodes, the CV curves were investigated to study the electrochemical kinetics and Zn^{2+}-storage behavior. Fig. 5a displays the CV curves of the Cu-VO_x electrode at various scan rates of 0.2, 0.3, 0.4, 0.6, 0.8, and 1 mV s^{-1}, respectively. It is clear that with increasing the scan rate, the peak current response became faster. However, the CV curves maintained almost the same shape at different scan rates, indicating that the Cu-VO_x electrode demonstrated high electrochemical reversibility. The energy-storage mechanism of the Cu-VO_x electrode can be analyzed using eqn (1), where i corresponds to the peak current at different scan rates, ν represents the corresponding scan rate, and b is a variable parameter between 0.5 and 1.

$$i = a\nu^b \tag{1}$$

The energy storage was dominated by a diffusive process (battery behavior) when b = 0.5, whereas the b value of 1 indicated the surface-capacitance-controlled process (capacitive behavior).[50] As seen, the energy storage of the Cu-VO_x electrode was mostly controlled by the surface-capacitance process, as shown in Fig. 5b. Also, the b-values of peaks 1, 2, 3, 4 for the Cu-VO_x electrode were 0.84, 0.80, 0.72, and 0.92, respectively. The

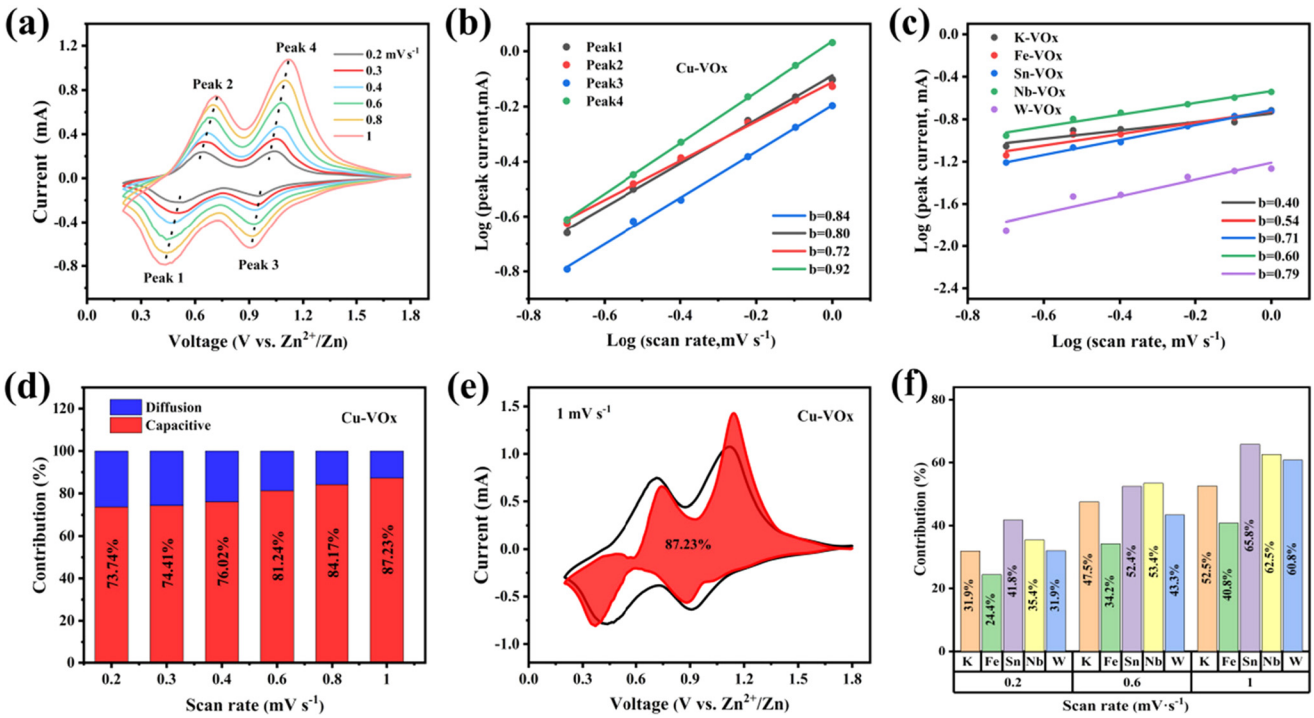

Fig. 5 (a) CV curves of the Cu-VO_x electrode at various scan rates ranging from 0.2 to 1 mV s^{-1}; (b and c) log(*i*) *vs.* log(*v*) plots of each electrode at specific peak currents of the CV curves; (e) CV curves of the Cu-VO_x electrode at 1.0 mV s^{-1}, showing the capacitive contribution to the total capacity (red region); (d and f) Capacities contributions of the capacitance-controlled and diffusion-limited processes of the Cu-VO_x, K-VO_x, Sn-VO_x, Nb-VO_x, Fe-VO_x, and W-VO_x electrodes, respectively.

b-values for the K-VO_x, Fe-VO_x, Sn-VO_x, Nb-VO_x, and W-VO_x electrodes are displayed in Fig. 4c for comparison, together with the corresponding analysis of the fitting for peak 1. The *b*-values of the K-VO_x and Fe-VO_x electrodes were 0.40 and 0.54, respectively. These suggested that surface pseudocapacitance processes dominate energy storage for the K-VO_x and Fe-VO_x electrodes, which was also consistent with their relatively low specific capacities as determined by analysis. The diffusion process dominated the energy-storage process for the Cu-VO_x electrode, which had a comparatively higher specific capacity and superior rate characteristic. The corresponding *b*-values of the Sn-VO_x, Nb-VO_x, and W-VO_x electrodes were 0.71, 0.60, and 0.79, respectively, as shown in Fig. S3† and Fig. 5c. Next, eqn (2), where (k_1v) denotes the energy obtained by the capacitive reaction and $(k_2v^{1/2})$ denotes the energy stored by the diffusion process, was used to conduct a more thorough analysis of the ratio of the capacitance-controlled and diffusion-controlled energy-storage processes for the Cu-VO_x electrode.[51]

$$i = k_1v + k_2v^{1/2} \tag{2}$$

The capacitance contributions of the Cu-VO_x, K-VO_x, Fe-VO_x, Sn-VO_x, Nb-VO_x, and W-VO_x electrodes at various scan rates are shown in Fig. 5d and f in detail. The surface capacitance contributions of the Cu-VO_x electrode were 73.74% at 0.2 mV s^{-1} and 87.23% at 1.0 mV s^{-1}, as shown in Fig. 5d. However, compared to the Cu-VO_x electrode at the same scanning rate of 1.0 mV s^{-1}, the capacitance contributions of the K-VO_x, Fe-VO_x, Sn-VO_x, Nb-VO_x, and W-VO_x electrodes were only 52.5%, 40.79%, 65.79%, 62.54%, and 60.79%, respectively. Therefore, the Cu-VO_x electrode exhibited excellent rate performances. The stronger bonding of Cu–O, the stable vanadium–oxygen skeleton, and excellent structural stability were responsible for the high surface capacitance contribution in the Cu-VO_x electrodes, which also improved their rate properties and cycling stability. Furthermore, the fitted CV plots of the Cu-VO_x electrode at 1.0 mV s^{-1} are displayed in Fig. 5e, where the CV curve with a surface capacitance contribution of 87.23% is displayed in the reddish-brown region.

The galvanostatic intermittent titration method (GITT) was used to further explore the reaction kinetics of the Cu-VO_x electrode. Fig. 6a displays the GITT curves of the Cu-VO_x electrode. This was accomplished by repeatedly charging and discharging the zinc-ion battery for 15 min with an 80 mA g^{-1} current pulse and then letting it rest for 1 h to allow the cell to relax. Also, the Zn^{2+}-diffusion coefficients (D_{Zn}^{2+}) for various charging and discharging states were computed using eqn (3):[52]

$$D_{Zn^{2+}} = \frac{4}{\pi\tau}L^2\left(\frac{\Delta E_S}{\Delta E_\tau}\right)^2 \tag{3}$$

where the value for the diffusion length (L) is equivalent to the electrode's thickness, ΔE_s represents the voltage change caused by the current pulse, and ΔE_t is the voltage evolution for galvanostatic discharging/charging, respectively. The Zn^{2+}-diffusion coefficients (D_{Zn}^{2+}) of the Cu-VO_x electrode are

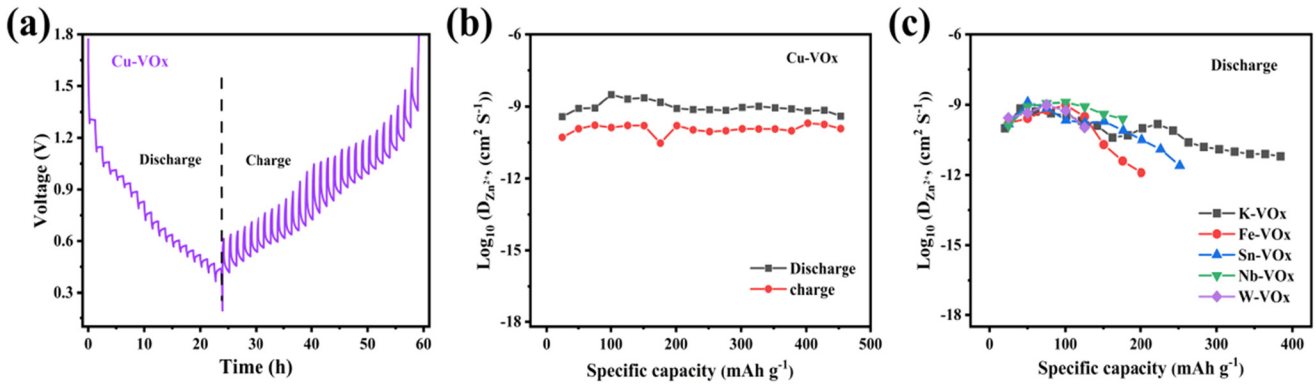

Fig. 6 (a and b) Discharging–charging GITT curves and corresponding ion-diffusion coefficients for the Cu-VO_x electrode; (c) corresponding ion-diffusion coefficients for the discharging GITT curves for the K-VO_x, Fe-VO_x, Sn-VO_x, Nb-VO_x, and W-VO_x electrodes, respectively.

depicted in Fig. 6b, which illustrate the charging and discharging process. With the ongoing the discharging and charging process, the diffusion coefficient kept in a stable state. It fluctuated between 9.42×10^{-9} and 8.51×10^{-8} cm^{-2} s^{-1} in the discharging state and between 9.69×10^{-9} and 1.05×10^{-10} cm^{-2} s^{-1} in the charging state. Additionally, as shown in Fig. 6c, the diffusion coefficients of the K-VO_x, Fe-VO_x, Sn-VO_x, Nb-VO_x, and W-VO_x electrodes all decreased to a greater extent after 10 h, which may be because the material structure collapsed as the number of cycles increased.[53–56] Also, the initial diffusion coefficients of the K-VO_x, Fe-VO_x, Sn-VO_x, Nb-VO_x, and W-VO_x electrodes were smaller than that of the Cu-VO_x electrode in the discharging state. Cu^{2+} pre-embedding in VO_x framework could improve the Zn^{2+}-diffusion rate and reaction kinetics, according to the computed results for the Cu-VO_x electrode, with superior performance compared to the earlier results based on vanadium-based cathodes.

4. Conclusions

In this work, a one-step hydrothermal reaction was used to design and successfully prepare different valence metal pre-embedding VO_x materials. Also, the pre-embedding of different metal ions was performed and had a great influence on the electrochemical performances of the VO_x compounds. Compared to the contrast electrodes, the Cu-VO_x electrode achieved excellent electrochemical performance, with a specific capacity of about 455.9 mA h g^{-1} at 0.1 A g^{-1} and it maintained a high specific capacity of 357.0 mA h g^{-1} over 200 charging/discharging cycles. Surprisingly, the Cu-VO_x electrode demonstrated 178.8 mA h g^{-1} at a high current density of 6 A g^{-1} and maintained 128 mA h g^{-1} over 2000 cycles, showing excellent rate performance. Cu^{2+} pre-embedding in VO_x introduced abundant oxygen vacancies and increased the interlayer distance, which improved the electrical conductivity and structural stability to accelerate the reaction kinetics. In addition, Cu^{2+} pre-embedding weakened the binding energy of the V–O bonds, making it easier for Cu-VO_x to maintain structural stability during charging/discharging cycles. On the other hand, the construction of thin sheet microspheres composed of nanoparticles increased the structural stability and shortened the distance for ion transport, enabling the Cu-VO_x electrode to demonstrate high rate characteristics and a long cycling lifespan. This design strategy provides a reference for the design of cathode materials with high electrochemical performances and can accelerate the commercial application of aqueous zinc-ion batteries.

Author contributions

Juan Xu: methodology, validation, writing original draft. Nengneng Han: conceptualization, investigation, editing. Sihao Chen: conceptualization, investigation. Yahui Zhang: conceptualization, investigation. Yuezhou Jing: conceptualization, investigation. Pibin Bing: conceptualization, editing. Zhongyang Li: conceptualization, review & editing.

Data availability

Data for this article, including [description of data types] are available at [name of repository] at [URL – format **https://doi.org/10.1039/d4dt01415d**].

Conflicts of interest

All the authors discussed the results and commented on the manuscript. And, the authors declared that they have no known competing financial interests.

Acknowledgements

This work was financially supported by the Doctoral Research Grant of the North China University of Water Resources and Electric Power and National Natural Science Foundation of China (No. 21875080).

References

1 H. Niu, N. Zhang, Y. Lu, Z. Zhang, M. Li, J. Liu, N. Zhang, W. Song, Y. Zhao and Z. Miao, Strategies toward the development of high-energy-density lithium batteries, *J. Energy Storage*, 2024, **88**, 111666.

2 J. Liu, Y. Zhang, J. Zhou, Z. Wang, P. Zhu, Y. Cao, Y. Zheng, X. Zhou, C. Yan and T. Qian, Advances and prospects in improving the utilization efficiency of lithium for high energy density lithium batteries, *Adv. Funct. Mater.*, 2023, **33**, 2302055.

3 S. Huo, L. Sheng, W. Xue, L. Wang, H. Xu, H. Zhang, B. Su, M. Lyu and X. He, Challenges of stable ion pathways in cathode electrode for all-solid-state lithium batteries: A Review, *Adv. Energy Mater.*, 2023, **13**, 2204343.

4 T. Bashir, S. Zhou, S. Yang, S. A. Ismail, T. Ali, H. Wang, J. Zhao and L. Gao, Progress in 3D-MXene electrodes for lithium/sodium/potassium/magnesium/zinc/aluminum-ion batteries, *Electrochem. Energy Rev.*, 2023, **6**, 5.

5 Q. Zhang, Q. Ma, R. Wang, Z. Liu, Y. Zhai, Y. Pang, Y. Tang, Q. Wang, K. Wu, H. Wu, Y. Zhang, L. Zhang, C. Zhang, L. Fu, S. Eliseeva, V. Kondratiev and Y. Wu, Recent progress in advanced organosulfur cathode materials for rechargeable lithium batteries, *Mater. Today*, 2023, **65**, 100–121.

6 F. Zhai, Q. Zhou, Z. Lv, Y. Wang, X. Zhou and G. Cui, Customized design of electrolytes for high-safety and high-energy-density lithium batteries, *EnergyChem*, 2022, **4**, 100082.

7 P. Shi, Z. H. Fu, M. Y. Zhou, X. Chen, N. Yao, L. P. Hou, C. Z. Zhao, B. Q. Li, J. Q. Huang, X. Q. Zhang and Q. Zhang, Inhibiting intercrystalline reactions of anode with electrolytes for long-cycling lithium batteries, *Sci. Adv.*, 2022, **8**, 3445–3455.

8 T. Zhou, L. Zhu, L. Xie, Q. Han, X. Yang, L. Chen, G. Wang and X. Cao, Cathode materials for aqueous zinc-ion batteries: A mini review, *J. Colloid Interface Sci.*, 2022, **605**, 828–850.

9 X. Zhang, Q. Shen, X. Lin, C. Luo, Y. Shen and X. Huang, Ion-confinement effect for zinc anode of aqueous zinc ion batteries, *J. Energy Storage*, 2023, **73**, 109085.

10 Y. Liu, L. Li, X. Ji and S. Cheng, Scientific challenges and improvement strategies of Zn-based anodes for aqueous Zn-ion batteries, *Chem. Rec.*, 2022, **22**, 202200114.

11 Y. Dai, C. Zhang, J. Li, X. Gao, P. Hu, C. Ye, H. He, J. Zhu, W. Zhang, R. Chen, W. Zong, F. Guo, I. P. Parkin, D. J. L. Brett, P. R. Shearing, L. Mai and G. He, Inhibition of vanadium cathodes dissolution in aqueous Zn-ion batteries, *Adv. Mater.*, 2024, **36**, 2310645.

12 N. Zhang, J. C. Wang, Y. F. Guo, P. F. Wang, Y. R. Zhu and T. F. Yi, Insights on rational design and energy storage mechanism of Mn-based cathode materials towards high performance aqueous zinc-ion batteries, *Coord. Chem. Rev.*, 2023, **479**, 215009.

13 Y. Zeng, X. F. Lu, S. L. Zhang, D. Luan, S. Li and X. W. Lou, Construction of Co-Mn prussian blue analog hollow spheres for efficient aqueous Zn-ion batteries, *Angew. Chem., Int. Ed.*, 2021, **60**, 22189–22194.

14 T. Jin, X. Ye, Z. Chen, S. Bai and Y. Zhang, Low-temperature and high-performance vanadium-based aqueous Zinc-ion batteries, *ACS Appl. Mater. Interfaces*, 2024, **16**, 4729–4740.

15 J. Zhang, W. Li, J. Wang, X. Pu, G. Zhang, S. Wang, N. Wang and X. Li, Engineering p-band center of oxygen boosting H^+ intercalation in δ-MnO_2 for aqueous zinc ion batteries, *Angew. Chem., Int. Ed.*, 2023, **62**, 202215654.

16 Y. Xu, G. Zhang, J. Liu, J. Zhang, X. Wang, X. Pu, J. Wang, C. Yan, Y. Cao, H. Yang, W. Li and X. Li, Recent advances on challenges and strategies of manganese dioxide cathodes for aqueous zinc-ion batteries, *Energy Environ. Mater.*, 2023, **6**, 12575.

17 Y. Zhang, R. Huang, X. Wang, Z. Wang, B. Song, Y. Du, Q. Lu, X. Chen and J. Sun, Facile large-scale preparation of vanadium pentoxide-polypyrrole composite for aqueous zinc-ion batteries, *J. Alloys Compd.*, 2022, **907**, 164434.

18 J. Wu, L. Yang, S. Wang, X. Yao, J. Wang, A. Abliz, X. Xie, H. Mi and H. Li, Zinc ion modulation of hydrated vanadium pentoxide for high-performance aqueous zinc ion batteries, *J. Power Sources*, 2024, **595**, 234057.

19 Y. Jiang, J. Lu, W. Liu, C. Xing, S. Lu, X. Liu, Y. Xu, J. Zhang and B. Zhao, Novel polymer/barium intercalated vanadium pentoxide with expanded interlayer spacing as high-rate and durable cathode for aqueous Zinc-ion batteries, *ACS Appl. Mater. Interfaces*, 2022, **14**, 17415–17425.

20 J. Chen, X. Hou, X. Wang, C. Wang, J. Wen, Y. Bu, G. Huang, T. Cao and S. Xu, Bi-intercalated vanadium pentoxide synthesized via hydrogen peroxide-induced phase transition for highly stable cathode in aqueous zinc ion batteries, *J. Mater. Chem. A*, 2024, 11322–11331.

21 F. Wu, Y. Wang, P. Ruan, X. Niu, D. Zheng, X. Xu, X. Gao, Y. Cai, W. Liu, W. Shi and X. Cao, Fe-doping enabled a stable vanadium oxide cathode with rapid Zn diffusion channel for aqueous zinc-ion batteries, *Mater. Today Energy*, 2021, **21**, 100842.

22 A. Wang, D. H. Liu, L. Yang, F. Xu, D. Luo, H. Dou, M. Song, C. Xu, B. Zhang, J. Zheng, Z. Chen and Z. Bai, Building stabilized $Cu_{0.17}Mn_{0.03}V_2O_5{\cdot}2.16H_2O$ cathode enables an outstanding room-/low-temperature aqueous Zn-ion batteries, *Carbon Energy*, 2024, **512**, 512–523.

23 Z. Pang, B. Ding, J. Wang, Y. Wang, L. Xu, L. Zhou, X. Jiang, X. Yan, J. P. Hill, L. Yu and Y. Yamauchi, Metal-ion inserted vanadium oxide nanoribbons as high-performance cathodes for aqueous zinc-ion batteries, *Chem. Eng. J.*, 2022, **446**, 136861.

24 Y. Tong, S. Su, X. Li, B. Liang, J. Peng, J. Hou and M. Luo, Synergistic iron ion and alkylammonium cation intercalated vanadium oxide cathode for highly efficient aqueous zinc ion battery, *J. Power Sources*, 2022, **528**, 231226.

25 X. Pang, S. Ji, P. Zhang, W. Feng, L. Zhang, K. Li, Y. Tang and Y. Liu, Interlayer doping of pseudocapacitive hydrated vanadium oxide via Mn^{2+} for high-performance aqueous zinc-ion battery, *Electrochim. Acta*, 2023, **441**, 141810.

26 Y. Qi, J. Huang, L. Yan, Y. Cao, J. Xu, D. Bin, M. Liao and Y. Xia, Towards high-performance aqueous zinc-ion battery via cesium ion intercalated vanadium oxide nanorods, *Chem. Eng. J.*, 2022, **442**, 136349.

27 J. Guan, L. Shao, L. Yu, S. Wang, X. Shi, J. Cai and Z. Sun, Two-dimensional $Mg_{0.2}V_2O_5{\cdot}nH_2O$ nanobelts derived from V_4C_3 MXenes for highly stable aqueous zinc ion batteries, *Chem. Eng. J.*, 2022, **443**, 136502.
28 H. Geng, M. Cheng, B. Wang, Y. Yang, Y. Zhang and C. C. Li, Electronic structure regulation of layered vanadium oxide via interlayer doping strategy toward superior high-rate and low-temperature Zinc-ion batteries, *Adv. Funct. Mater.*, 2020, **30**, 1907684.
29 Q. Sun, H. Cheng, C. Sun, Y. Liu, W. Nie, K. Zhao, X. Lu and J. Zhou, Architecting a hydrated $Ca_{0.24}V_2O_5$ cathode with a facile desolvation interface for superior-performance aqueous zinc ion batteries, *ACS Appl. Mater. Interfaces*, 2021, **13**, 60035–60045.
30 M. Tian, C. Liu, J. Zheng, X. Jia, E. P. Jahrman, G. T. Seidler, D. Long, M. Atif, M. Alsalhi and G. Cao, Structural engineering of hydrated vanadium oxide cathode by K^+ incorporation for high-capacity and long-cycling aqueous zinc ion batteries, *Energy Storage Mater.*, 2020, **29**, 9–16.
31 L. Wang, K. W. Huang, J. Chen and J. Zheng, Ultralong cycle stability of aqueous zinc-ion batteries with zinc vanadium oxide cathodes, *Sci. Adv.*, 2019, **5**, 4279–4288.
32 J. Xu, Y. Zhang, C. Liu, H. Cheng, X. Cai, D. Jia and H. Lin, Al^{3+} introduction hydrated vanadium oxide induced high performance for aqueous zinc-ion batteries, *Small*, 2022, **18**, 2204180.
33 Y. Zou, Z. Guo, J. Zhou, Q. Zheng, X. Shan and L. Zhao, One-pot preparation of La(OH)3 nanoparticles and NiMn LDH nanosheets with mutual support structure as cathode for high-performance aqueous zinc-ion batteries, *J. Alloys Compd.*, 2022, **918**, 165547.
34 Y. Zhang, S. Jiang, Y. Li, X. Ren, P. Zhang, L. Sun and H. Y. Yang, In situ grown hierarchical electrospun nanofiber skeletons with embedded vanadium nitride nanograins for ultra-fast and super-long cycle life aqueous Zn-ion Batteries, *Adv. Energy Mater.*, 2023, **13**, 2370021.
35 B. Yang, H. Quan, J. Gao, S. Wang, N. Wang and C. Sun, MnO nanoparticles with cationic defects encapsulated in nitrogen-doped porous carbon for high-performance aqueous zinc-ion batteries, *J. Alloys Compd.*, 2021, **889**, 161680.
36 S. Tan, Z. Sang, Z. Yi, J. Guo, X. Zhang, P. Li, W. Si, J. Liang and F. Hou, Conductive coating, cation-intercalation, and oxygen vacancies co-modified vanadium oxides as high-rate and stable cathodes for aqueous zinc-ion batteries, *EcoMat*, 2023, **5**, 12326.
37 C. Li, C. Zheng, H. Jiang, S. Bai and J. Jia, Conductive flower-like Ni-PTA-Mn as cathode for aqueous zinc-ion batteries, *J. Alloys Compd.*, 2021, **882**, 160587.
38 Q. Jiao, T. Zhou, N. Zhang, S. Liu, Q. Huang, W. Bi, W. Chu, X. Wu, Y. Zhu, Y. Feng and C. Wu, High-surface-area titanium nitride nanosheets as zinc anode coating for dendrite-free rechargeable aqueous batteries, *Sci. China Mater.*, 2022, **65**, 1771–1778.
39 G. Qu, K. Guo, W. Chen, Y. Du, Y. Wang, B. Tian and J. Zhang, Cs-induced phase transformation of vanadium oxide for high-performance zinc-ion batteries, *Energy Environ. Mater.*, 2023, **6**, 12502.
40 H. Zhang, Y. Rong, W. Jia, H. Chai and Y. Cao, Simple solvent-free synthesis of rod-like Cu-doped V_2O_5 for high storage capacity cathode materials of lithium ion batteries, *J. Alloys Compd.*, 2019, **802**, 139–145.
41 L. Xu, Y. Zhang, J. Zheng, H. Jiang, T. Hu and C. Meng, Ammonium ion intercalated hydrated vanadium pentoxide for advanced aqueous rechargeable Zn-ion batteries, *Mater. Today Energy*, 2020, **18**, 100509.
42 J. Qian, Y. You, Z. Fan, X. Liu, J. Tang, W. He and Z. Sun, Mn pre-intercalated hydrated vanadium pentoxide activated by nitrogen plasma for enhanced zinc ion storage, *J. Energy Storage*, 2023, **63**, 106988.
43 Y. Fang, Y. Chen, L. Zeng, T. Yang, Q. Xu, Y. Wang, S. Zeng, Q. Qian, M. Wei and Q. Chen, Nitrogen-doped carbon encapsulated zinc vanadate polyhedron engineered from a metal-organic framework as a stable anode for alkali ion batteries, *J. Colloid Interface Sci.*, 2021, **593**, 251–265.
44 H. Yan, C. Yang, L. Zhao, J. Liu, P. Zhang and L. Gao, Proton-assisted mixed-valence vanadium oxides cathode with long-term stability for rechargeable aqueous zinc ion batteries, *Electrochim. Acta*, 2022, **429**, 141003.
45 C. Liu, Z. Neale, J. Zheng, X. Jia, J. Huang, M. Yan, M. Tian, M. Wang, J. Yang and G. Cao, Expanded hydrated vanadate for high-performance aqueous zinc-ion batteries, *Energy Environ. Sci.*, 2019, **12**, 2273–2285.
46 Z. Yao, D. Cai, Z. Cui, Q. Wang and H. Zhan, Strongly coupled zinc manganate nanodots and graphene composite as an advanced cathode material for aqueous zinc ion batteries, *Ceram. Int.*, 2020, **46**, 11237–11245.
47 Y. Liu, C. Gao, Y. Sun, X. Hao, Z. Pi, M. Yang, X. Zhao and K. Cai, Enhancing the electrochemical activation kinetics of V_2O_3 for high-performance aqueous zinc-ion battery cathode materials, *Chem. Eng. J.*, 2024, 151535.
48 T. Zhou and G. Gao, Pre-intercalation strategy in vanadium oxides cathodes for aqueous zinc ion batteries: Review and prospects, *J. Energy Storage*, 2024, **84**, 110808.
49 X. Chen, W. Li, D. Reed, X. Li and X. Liu, On energy storage chemistry of aqueous Zn-ion batteries: From cathode to anode, *Electrochem. Energy Rev.*, 2023, **6**, 33.
50 J. Xu, H. Guo, Z. Li, H. Xu, N. Han, S. Chen and K. Huo, Carbon coated Mo-doped MnSx nanoparticles integrating with sulfur vacancies as cathode for improved zinc ions storage, *J. Alloys Compd.*, 2023, **945**, 169191.
51 J. Xu, H. Guo, Z. Li, K. Huo and G. Ma, Unique $CoWO_4@WO_3$ heterostructured nanosheets with superior electrochemical performances for all-solid-state supercapacitors, *Dalton Trans.*, 2022, **51**, 12299–12306.
52 H. Luo, L. Wang, P. Ren, J. Jian, X. Liu, C. Niu and D. Chao, Atomic engineering promoted electrooxidation kinetics of manganese-based cathode for stable aqueous zinc-ion batteries, *Nano Res.*, 2022, **15**, 8603–8612.

53 K. Zhu, Z. Sun, P. Liu, H. Li, Y. Wang, K. Cao and L. Jiao, Intercalation engineering of layered vanadyl phosphates for high performance zinc-ion batteries, *J. Energy Chem.*, 2021, **63**, 239–245.
54 L. Wang, Z. Cao, P. Zhuang, J. Li, H. Chu, Z. Ye, D. Xu, H. Zhang, J. Shen and M. Ye, Electrochemical injection oxygen vacancies in layered $Ca_2Mn_3O_8$ for boosting zinc-ion storage, *ACS Appl. Mater. Interfaces*, 2021, **13**, 13338–13346.
55 H. Wang, R. Jing, J. Shi, M. Zhang, S. Jin, Z. Xiong, L. Guo and Q. Wang, Mo-doped $NH_4V_4O_{10}$ with enhanced electrochemical performance in aqueous Zn-ion batteries, *J. Alloys Compd.*, 2021, **858**, 158380.
56 Q. Li, X. Ye, H. Yu, C. Du, W. Sun, W. Liu, H. Pan and X. Rui, Pre-potassiated hydrated vanadium oxide as cathode for quasi-solid-state zinc-ion battery, *Chin. Chem. Lett.*, 2022, **33**, 2663–2668.

